

Laser power consumption of soliton formation in a bidirectional Kerr resonator

Received: 12 June 2024

Accepted: 14 January 2025

Published online: 05 March 2025

 Check for updates

Jizhao Zang ^{1,2}✉, Su-Peng Yu^{1,2}, Haixin Liu ^{1,2}, Yan Jin ^{1,2}, Travis C. Briles¹, David R. Carlson^{1,3} & Scott B. Papp^{1,2}

Laser sources power ultrafast data transmission, computing acceleration, access to ultra-high-speed signalling, and sensing applications such as chemical detection, distance measurements and pattern recognition. The ever-growing scale of these applications drives innovation in multiwavelength lasers for massively parallel processing. We report a nanophotonic Kerr-resonator circuit that converts the power of an input laser into a normal-dispersion soliton frequency comb at approaching unit efficiency. By coupling forward and backward propagation, we realize a bidirectional Kerr resonator that supports universal phase matching but also opens excess loss by double-sided emission. We therefore induce reflection of the resonator's forward, external coupling port to favour backward propagation, resulting in efficient, unidirectional soliton formation. Coherent backscattering with nanophotonics provides the control to put arbitrary phase-matching and efficient laser power consumption on equal footing in Kerr resonators. In the overcoupled-resonator regime, we measure 65% conversion efficiency for a 40 mW input pump laser; the nonlinear circuit consumes 97% of the pump, generating the maximum possible comb power. Our work opens up high-efficiency soliton formation in integrated photonics, exploring how energy flows in nonlinear circuits and enabling laser sources for applications such as advanced transmission, computing, quantum sensing and artificial intelligence.

Nonlinear optics is a ubiquitous phenomenon in science and technology that converts light from one wavelength to another and enables the synthesis of new optical fields. Development in nonlinear optics has advanced a host of applications, ranging from optical signal processing¹, to ultra-short pulsed lasers² and optical parametric amplifiers^{3–5}, to quantum-state generation and manipulation^{6–10}. Invariably, nonlinear effects are relatively weak, and harnessing their benefits stimulates progress in engineering the control of light–matter interactions. Given that third-order Kerr-effect nonlinearity, which involves an intensity-dependent refractive index, occurs in practically all materials, it is widely used in scalable technologies such as integrated photonics^{11–15}.

Controlling Kerr nonlinearity in microresonators is a central goal for integrated photonics. The high quality factor and small mode volume of microresonators make optical parametric oscillation possible with a threshold power of much less than 1 mW (ref. 16), enabling the use with many different types of lasers. Moreover, adjusting the material and shape of a microresonator enables phase-matching for four-wave mixing (FWM). There now exists a fundamental understanding of stability criteria for many types of nonlinear field states in Kerr microresonators, including parametric oscillation^{17–19} and soliton microcombs^{14,20–22}. We consider the latter as self-reinforcing, temporally localized pulses in a resonator that manifest as a frequency comb

¹Time and Frequency Division, National Institute of Standards and Technology, Boulder, CO, USA. ²Department of Physics, University of Colorado, Boulder, CO, USA. ³Octave Photonics, Louisville, CO, USA. ✉e-mail: jizhao.zang@nist.gov

at the resonator output. Soliton stability and generation has recently been enhanced by coupling forward and backward propagation in microresonators as an added mechanism to control nonlinear phase matching. Photonic-crystal resonator (PhCR) microcombs^{23–25} implement coherent scattering with subwavelength nanopatterns to realize a bidirectional Kerr resonator, and self-injection-locked microcombs exploit direct laser-resonator feedback^{26–30}. These bidirectional systems can feature universal phase matching in any dispersion regime and spontaneous soliton formation.

Although phase-matching is essential for initiating nonlinear field states such as soliton microcombs, efficiently energizing and harvesting the soliton comb requires a distinct set of physical optimizations. High pump-to-comb conversion efficiency (CE) increases the power per comb mode, which is critical for applications such as wavelength-division-multiplexing transceivers^{31,32} and microwave photonic filters³³. To maximize CE, first, the external coupling rate (κ_c) of the microresonator must be larger than the internal loss rate (κ_i). Furthermore, phase-matching constrains the CE of solitons by limiting the range of system parameters such as laser detuning. Still, isolated, high CE soliton states have been reported. Efficient temporal solitons have been demonstrated in coupled-fibre cavities³⁴ and a microresonator nested in a fibre loop with gain³⁵, but such systems are incompatible with chip-scale integration. Soliton crystals achieve nearly unit CE by exciting several solitons in one resonator; however, destructive interference reduces the utility of such ensembles³⁶. Solitons in anomalous-dispersion resonators with shifted pump resonance offer a path to high efficiency. A conversion efficiency of beyond 50% was achieved in 100 GHz solitons, and wafer-level manufacturing of such microcombs has been demonstrated with a 98% yield^{37,38}. However, precise control of the pump laser and auxiliary cavity is required to initiate the soliton state. Solitons in normal-dispersion resonators^{39,40} can leverage a long duty cycle for enhanced CE and resonator thermal stability for soliton formation. A 200 GHz microcomb with 41% CE and a 105 GHz microcomb with 49% CE have been reported^{41,42}, but the soliton phase-matching range is limited or needs tuning with avoided mode crossings. Hence, unified control of phase-matching and CE for high pump-laser consumption in solitons is an outstanding objective.

Here we leverage coherent scattering in a nanophotonic Kerr-resonator circuit to provide universal phase-matching for soliton microcombs and demonstrate deterministic control of CE up to the unit boundary. We experimentally generate solitons with a PhCR that features normal dispersion and one ‘split mode’ with coherently coupled forward and backward propagation. The mode splitting can be varied to >100 GHz for near-arbitrary phase matching. Moreover, this direct phase matching enables a continuous evolution from the empty resonator state to a backward-propagating soliton. However, CE in a bidirectional resonator cannot exceed 50% because the localized soliton circulates in one direction while the pump is distributed in both. We place a reflector on the coupling waveguide to consume the forward pump power and close off excess loss of the double-sided resonator. Our nanophotonic soliton circuit emits a 200 GHz train of flat-top pulses with up to 65% CE and 97% pump consumption. Moreover, the nanophotonic circuit enables precise control of the comb spectrum that we use for alignment to the ITU-T grid, with <2.6 GHz offset and compatibility with a distributed feedback (DFB) laser diode on the 193.1 THz channel. Our work demonstrates near-unit efficiency comb generation with a bidirectional Kerr resonator by controlling pump utilization with on-chip nanophotonics, enabling, for example, massive scaling in data transmission and processing.

Figure 1 introduces the structure of our nanophotonic resonator circuit, with emphasis on how we achieve unified control of phase-matching and CE through coherent backscattering. The circuit (Fig. 1a) is composed of: a PhCR in which the ring width is modulated with a periodicity of $\pi a/m$, where a is the PhCR radius and m is the azimuthal mode number; an evanescent coupling waveguide curved

around the PhCR for enhanced escape efficiency; and a reflector in the coupling waveguide, in which the waveguide width is modulated with a periodicity of $\Lambda = \pi c/\omega_l n_{\text{eff}}$, where c is the speed of light, ω_l is the laser frequency and n_{eff} is the effective refractive index. We denote PhCR mode m as the split mode, which manifests as two resonances split in frequency by the bandgap ϵ due to the coherently coupled forward and backward propagation. To energize a soliton in a normal-dispersion PhCR, we tune the pump laser into the lower frequency resonance of the split mode, which creates localized anomalous dispersion to break the continuous-wave state via modulation instability. The higher-frequency resonance of the split mode does not offer phase-matching for FWM because the adjacent PhCR modes are all at lower frequencies. As we induce almost complete reflection over a 3 dB bandwidth of 7.6 THz, the forward-propagating pump laser and backward-propagating soliton microcomb combine at a circulator and couple to the chip at a common facet. We envision that chip-scale circulators can be implemented using non-reciprocal Kerr nonlinear ring resonators⁴³. Alternatively, we can use on-chip spectral filters^{44,45} to separate the forward-propagating pump and backward-propagating combs. We implement the circuit on a silicon chip by use of conventional semiconductor processing with the tantalum pentoxide (Ta_2O_5 , hereafter tantala) material platform. We perform nanofabrication on a 75 mm wafer with <150 nm feature resolution in the tantala device layer, creating 50 chips with 100 circuit variations per chip for experiments^{23,46–48}. Both the PhCR and the reflector are periodic structures with a periodicity of approximately 450 nm. Features of this size range are well within the resolution of modern commercially available lithography tools. Figure 1b shows scanning electron microscope images of the nanophotonic circuit elements, emphasizing the modulation on the inner edge of the PhCR and the width-modulated waveguide that forms the reflector.

We consider the forward and backward-propagating fields to understand operation of the nanophotonic circuit (see Fig. 1c). Coherent scattering in the PhCR creates a bidirectional pump that in principle supports simultaneous excitation of solitons in the forward and backward directions; however, backward operation shows higher gain and is favoured over forward operation²⁵. Hence, the pump laser in the forward direction is not used. The function of the reflector is to reflect the forward pump field and constructively interfere with the backward pump field in the PhCR. We characterize the phase delay ϕ of the reflected pump with respect to the PhCR, and operationally, we control ϕ by rotating the PhCR with respect to the coupling waveguide.

We explore the dynamics and steady-state field solution of the PhCR with the Lugiato–Lefever equation (LLE)⁴⁹, including the forward-backward coupling and the pump reflector that we implement through coherent scattering^{50,51}. Moreover, the LLE depends on dissipation, group-velocity dispersion and detuning of the pump laser. In particular,

$$\begin{aligned} \frac{\partial E_\mu^f}{\partial t} &= -(1 + i\alpha)E_\mu^f - i\frac{d_2}{2}\mu^2 E_\mu^f + i\mathcal{F}\left(|E_\mu^f|^2 E_\mu^f\right) + 2iE_\mu^f \sum_j |E_j^b|^2 \\ &\quad + \delta_{\mu 0} \left(F - \frac{i\epsilon_{\text{PhC}}}{2} E_\mu^b\right) \\ \frac{\partial E_\mu^b}{\partial t} &= -(1 + i\alpha)E_\mu^b - i\frac{d_2}{2}\mu^2 E_\mu^b + i\mathcal{F}\left(|E_\mu^b|^2 E_\mu^b\right) + 2iE_\mu^b \sum_j |E_j^f|^2 \\ &\quad + \delta_{\mu 0} \left(rF - \frac{i\epsilon_{\text{PhC}}}{2} E_\mu^f\right) - I_\alpha(\mu) \gamma r E_\mu^f \end{aligned} \quad (1)$$

where E_μ^f and E_μ^b are the forward and backward field amplitude in mode with index μ relative to the split mode. All frequency variables are normalized to the half-linewidth of the resonator $\kappa/4\pi$, where $\kappa = \kappa_i + \kappa_c$ is the total loss rate. The variable $\alpha = 2(\omega_l - \omega_0)/\kappa$ is the normalized detuning between ω_l and the split mode ω_0 . The parameter d_2 is the normalized group-velocity dispersion D_2 that is derived from the Taylor expansion of the resonance frequencies around $\omega_0: \omega_\mu = \omega_0 + D_1\mu + D_2\mu^2/2 + \dots$, where $D_1/2\pi$ is the free-spectral range (FSR). The

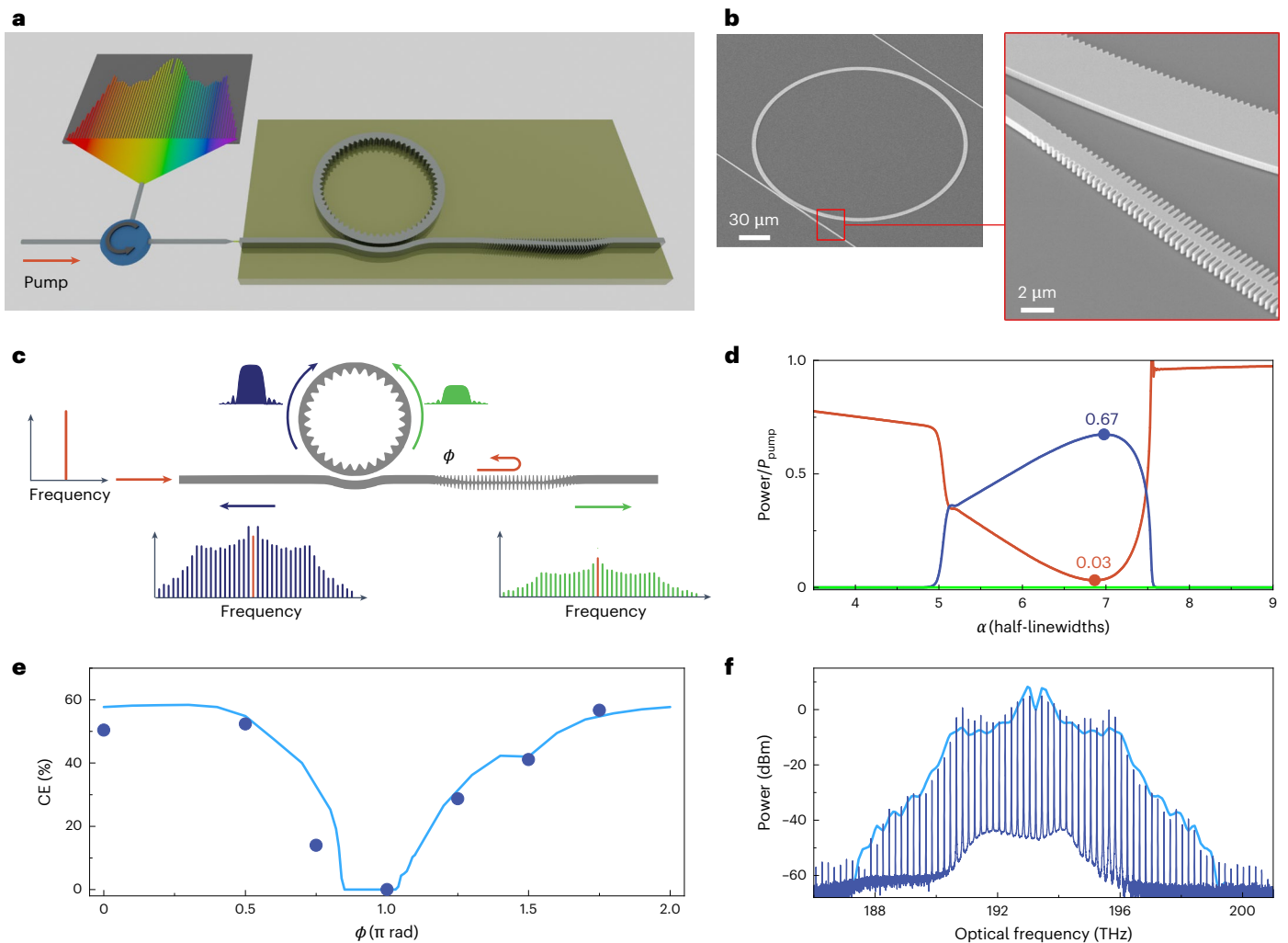


Fig. 1 | Soliton formation in the nanophotonic circuit. **a**, Schematic of the nanophotonic Kerr-resonator circuit with a PhCR and a waveguide reflector. **b**, Scanning electron microscope images of the nanophotonic structures. **c**, The bidirectional pump in the PhCR supports microcombs in the forward and backward directions. We tune ϕ for constructive interference between the

reflected and backward pumps in the PhCR. **d**, Power flow in the circuit analysed by LLE simulation with $(P_f + P_b)/P_{\text{pump}}$ (red), $P_{\text{comb}}^f/P_{\text{pump}}$ (green) and $P_{\text{comb}}^b/P_{\text{pump}}$ (blue). **e**, Measured CE versus ϕ (filled circles) and LLE simulation (solid curve). **f**, Measured (data trace) and simulated (line) optical spectrum of a soliton microcomb with a CE of 65%.

third and fourth terms of equation (1) represent self- and cross-phase modulation, respectively, where E^f and E^b are the temporal amplitudes of the intracavity field, and \mathcal{F}_μ represents the μ th frequency component of the Fourier series. In the forward and backward directions, different sources contribute to the pump power. In the forward direction, the pump power originates from the external laser on the coupling waveguide and the power coupled from E_0^b due to coherent backscattering in the PhCR. In the backward direction, the pump power originates from the external laser after travelling through the evanescent coupling region and being reflected, E_0^f that is outcoupled, reflected and coupled back into the PhCR, and coherent backscattering of E_0^f inside of the resonator. In the fifth term: $\delta_{\mu 0}$ is the Kronecker delta ($\delta_{00} = 1$, otherwise $\delta_{\mu 0} = 0$), $r = \sqrt{R} e^{i\phi}$ is the reflection coefficient of the waveguide reflector (where R is the reflectivity), F is the normalized amplitude of the pump, and $\epsilon_{\text{PhCR}} = 4\pi\epsilon/\kappa$ is the normalized ϵ . The transfer function from the resonator to the coupling waveguide is defined as $\gamma = 2K/(K+1)$, where K is the coupling factor. As the reflector has a finite reflection bandwidth, we apply an indicator function $I_\Omega(\mu)$: if $\mu \in \Omega$, $I_\Omega(\mu) = 1$, otherwise $I_\Omega(\mu) = 0$, where Ω is a set of μ that corresponds to the resonator modes in the reflection band. In the LLE simulation, we use $\Omega = \{-19, -18, \dots, 18, 19\}$ to model our nanophotonic circuit and we assume r is the same for $\mu \in \Omega$.

Using the LLE, we simulate power flow in the nanophotonic circuit to understand CE and pump laser consumption (Fig. 1d). We define CE as $\text{CE} = P_{\text{comb}}/P_{\text{pump}}$, where P_{pump} is the pump laser power and P_{comb} is the total emitted comb power. To quantify the power flow in both of the propagating directions on the coupling waveguide, we denote the comb power in the forward and backward directions as P_{comb}^f and P_{comb}^b , respectively, and the outcoupled pump in the forward and backward directions as P_f and P_b , respectively. Then, P_{comb} naturally becomes $P_{\text{comb}}^f + P_{\text{comb}}^b$. As a function of α , we simulate $(P_f + P_b)/P_{\text{pump}}$ (red), $P_{\text{comb}}^f/P_{\text{pump}}$ (green) and $P_{\text{comb}}^b/P_{\text{pump}}$ (blue) in the coupling waveguide. As the larger gain and the reflector favour backward soliton formation, both numerical simulations and experimental results show that the comb power in the backward direction is >20 dB higher than that in the forward direction. We therefore consider $P_{\text{comb}}^b \gg P_{\text{comb}}^f$ and $P_{\text{comb}} \approx P_{\text{comb}}^b$, unless otherwise specified. In the simulation, the optimal reflection phase for maximum CE is $\phi = 0$ rad. The other parameter of this simulation is K , which we set to a value of 4.5. As we inspect the simulated behaviour of soliton formation in this device in a similar fashion as we sweep α in the experiment, we observe initial consumption of the pump laser due to internal losses of the resonator. We subsequently observe rapid formation of the soliton, which reaches a CE and laser consumption of 67% and 97%, respectively. The soliton rapidly

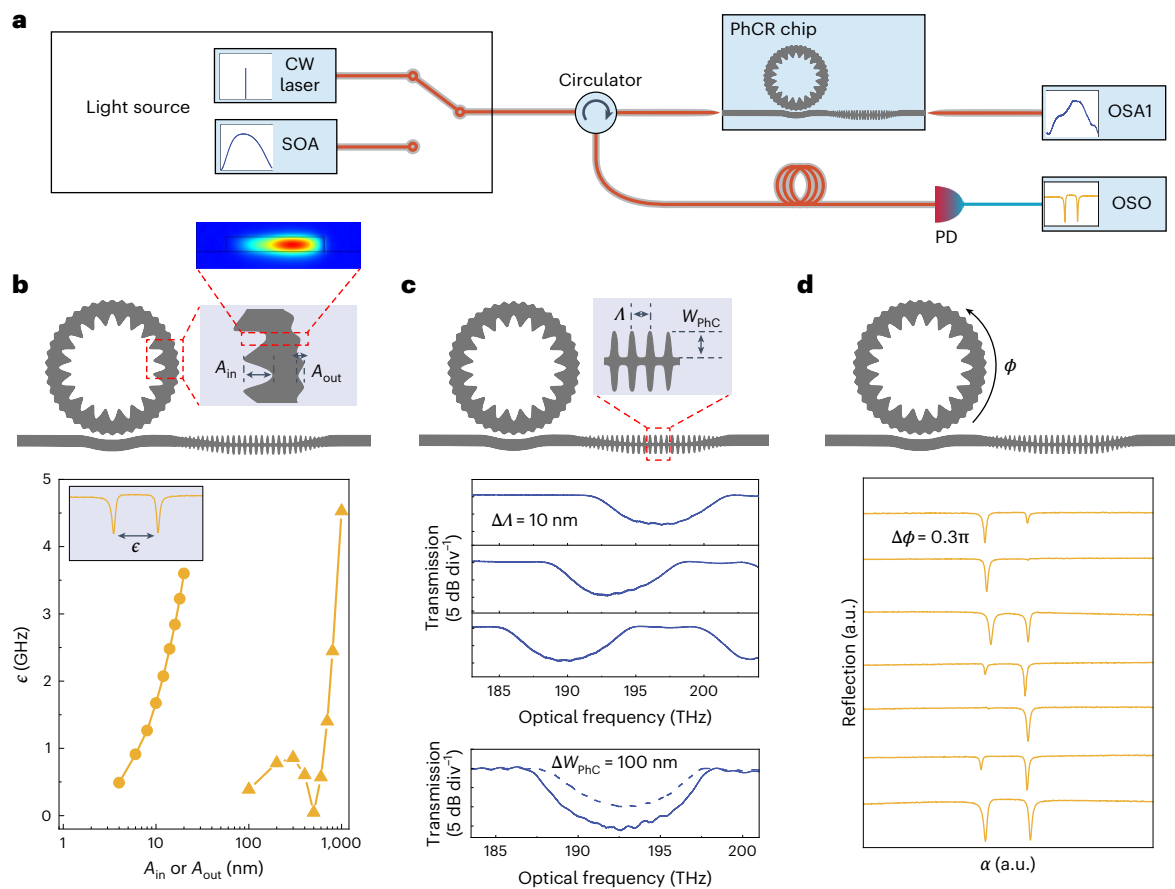


Fig. 2 | Characterization of the nanophotonic circuit structures. **a**, Set-up for device characterization. CW, continuous-wave; SOA, semiconductor optical amplifier; OSA, optical spectrum analyser; PD, photodetector; OSO, oscilloscope. **b**, The bandgap ϵ measured as a function of the modulation amplitude on the inner (A_{in} , triangles) or outer (A_{out} , circles) edge of the PhCR

($\alpha = 109.5 \mu\text{m}$, ring width = $4 \mu\text{m}$). The inset shows the transmission of a split mode. **c**, Optimization of the reflection band and R : transmission spectra of the reflector for varying $\Delta\lambda$ and W_{PhC} . **d**, Nanophotonic circuit reflection as we step ϕ in 0.3π increments.

de-energizes as α exceeds the range over which the soliton is stable in the resonator. These predicted behaviours are favourable for applications (particularly the high CE), which motivates us to explore soliton formation with fabricated versions of this system.

Our simulations indicate that ϕ is the critical parameter to access the regime of near-unit CE in our nanophotonic circuit. To explore this, we design a set of circuits on a common chip in which we systematically and precisely vary ϕ ; we then optimize CE by testing such copies of the circuit. Here, our test procedure is to scan α , record the reflection of the split mode to characterize the dependence of pump interference on ϕ , and then pump the lower frequency resonance of the split mode with the optimal ϕ .

Figure 1e presents measurements of CE (filled circles) in the nanophotonic circuit alongside the LLE simulation (solid curve) as a function of ϕ . The agreement between the simulation and experiment highlights our understanding of the system, our capability to accurately fabricate specific circuit designs with a set of ϕ values, and the robustness of the nonlinear nanophotonic circuit operation. The variation in ϕ results in constructive and destructive interference between the reflected forward pump by the reflector and backward pump in the PhCR, leading to different CEs in the nanophotonic circuit. Here we use $K = 3$ and the highest measured CE is 57% in the experimental data, but our simulation suggests that higher CE is possible with larger values of K . For example, we experimentally achieve a CE of 65% at $K = 4.5$ and $P_{\text{pump}} = 40$ mW. In Fig. 1f we present the optical frequency spectrum obtained by using this highest-CE device. We tune α to access this spectrum in which the mode-to-mode power variation is relatively small. The measured

soliton microcomb spectrum (data trace) is in agreement with the LLE simulation (line). We also observe substantial consumption of the pump laser in forming solitons, and the remaining pump power exiting the circuit is only 1 mW.

We present characterization of the nanophotonic circuit structures that control CE (Fig. 2). We use a narrow-linewidth laser to attain fine frequency resolution, and a broad-band light source to measure across the entire operating bandwidth of the circuit. We record optical signals with a standard optical spectrum analyser and a photodetector with an emphasis on the reflected power from the circuit (Fig. 2a).

As we show in Fig. 2b, we implement the azimuthal ring width modulation (A_{in} and A_{out}) on either the inner or outer edge of the PhCR, given that the overlap between the interactivity field and the nanopattern permits access to different ranges of modulation amplitude. With the PhCR, the number of modulation periods corresponds to twice m , the mode number of the PhCR mode that exhibits coherent backscattering, and the amplitude of the modulation controls ϵ of the split mode. We measure ϵ by a calibrated laser frequency scan across the split mode, and access to ϵ from zero to 5 GHz provides the range that our LLE simulations indicate are needed for soliton formation. To implement and test the reflector in the coupling waveguide, we tune λ so that the reflection band is centred on the split mode, and we optimize the amplitude of the nanopattern for $R > 90\%$. Figure 2c shows our operational procedure to optimize the reflection band as we vary λ to shift the frequency of maximum reflection. We observe this shift in the transmission spectra as we step λ in steps $\Delta\lambda = 10$ nm. This relatively coarse resolution in the nanopattern is sufficient to

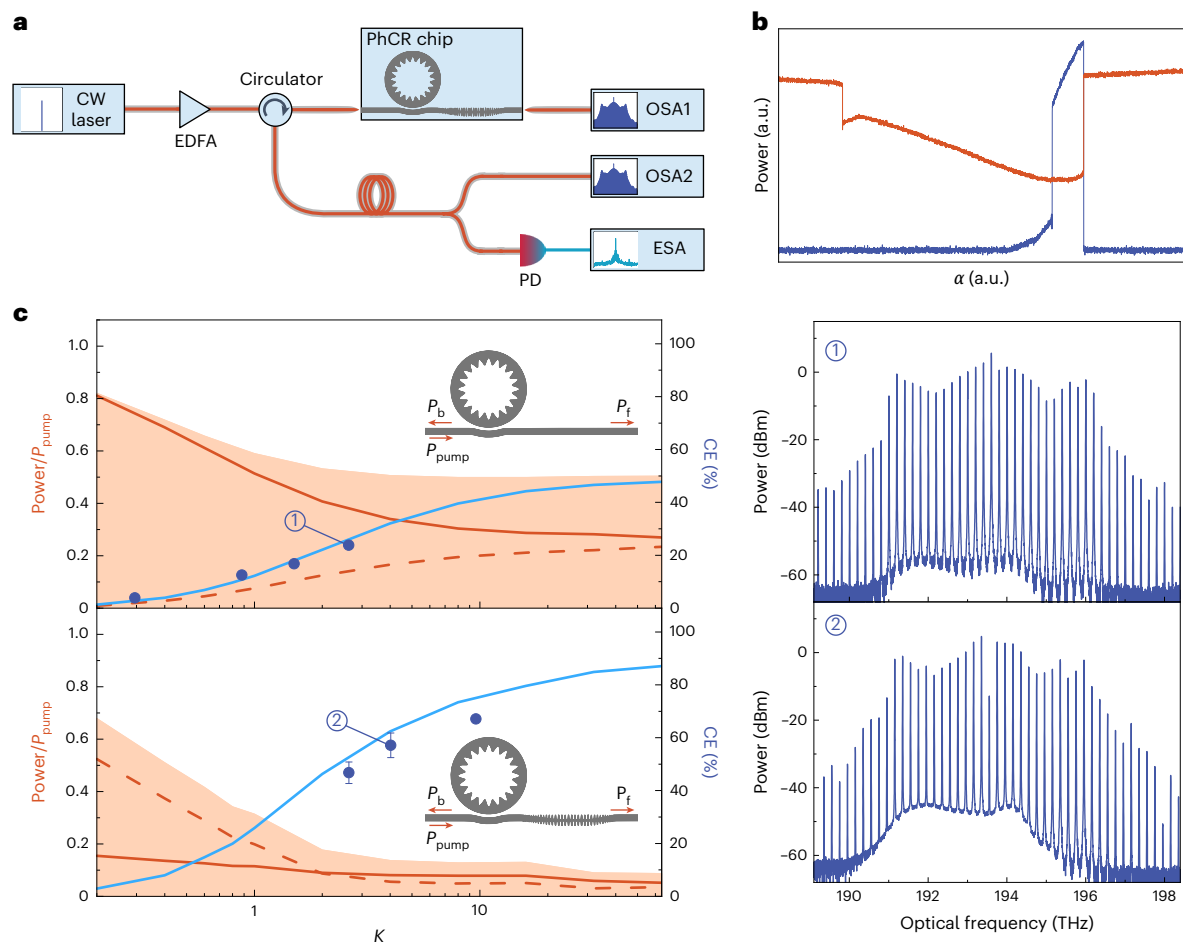


Fig. 3 | Laser power consumption and CE in the nanophotonic circuit. a.

Experimental set-up for soliton generation and characterization. CW, continuous-wave; EDFA, erbium-doped fibre amplifier; ESA, electrical spectrum analyser; OSA, optical spectrum analyser; PD, photodetector. **b.** Oscilloscope traces of P_b (red) and P_{comb}^b (blue) versus α . **c.** Comparison of unused pump power and CE between the scenarios in which $R = 0$ (upper panel) and $R = 0.9$ (lower panel). The insets show the definition of P_f , P_b , and P_{pump} for each scenario. The

plot includes P_f/P_{pump} (solid red line), P_b/P_{pump} (dashed red line), $(P_f + P_b)/P_{\text{pump}}$ (red shaded area), and CE (solid blue line), as a function of K in the LLE simulation. The filled blue circles represent the measured CE, whereas the panels to the right show the corresponding optical spectra of backward-propagating soliton microcombs. In the lower panel, the measured CEs are presented as mean values \pm s.d. ($n = 4$ for $K = 2.6$, $n = 3$ for $K = 4.0$).

align the split mode and peak R of the reflector. We also characterize the dependence of R on the amplitude of the reflector nanopattern; see the modulation depth W_{phc} in Fig. 2c. We vary R from 90% to 97% by adjusting W_{phc} from 750 nm to 850 nm.

With optimized reflection bandwidth and R , we characterize the intracavity pump power at the two resonances of the split mode. Figure 2d shows measurements of reflection from the nanophotonic circuit in which we incrementally vary ϕ in 0.3π steps. The data demonstrate the interference of the pump laser, specifically, that either the higher or lower frequency component of the split mode undergoes destructive interference. Due to the electric field profile in the PhCR, the two resonances are out of phase by π (ref. 23). Operationally, we vary ϕ by rotating the PhCR to change the alignment of the azimuthal nanopattern and the reflector. This procedure mitigates fabrication imperfections due to the rotational symmetry of the resonator. Another benefit of the reflector in our nanophotonic circuit is reduction in thermal instability from absorbed pump power in the resonator. At the optimal setting of ϕ , the higher-frequency resonance is not substantially excited and thus does not contribute to absorption and heating of the PhCR.

We explore the operation of our nanophotonic circuit by comparison to the case with $R = 0$ (Fig. 3). In both cases, the tantala PhCRs that we investigate have an intrinsic quality factor of $Q_i = \omega_0/\kappa_i = 2.7 \times 10^6$.

The device parameters are: $a = 109.5 \mu\text{m}$, ring width = $4 \mu\text{m}$, waveguide height = 570 nm , $A_{\text{in}} = 275 \text{ nm}$, $\text{FSR} = 200 \text{ GHz}$, $D_2 = -2\pi \times 8.5 \text{ MHz}$ and $\epsilon = 0.9 \text{ GHz}$. Our set-up for soliton generation and characterization is shown in Fig. 3a (see Supplementary Section 5 for more details). Here we use an erbium-doped fibre amplifier to boost the power of our tunable laser. We characterize soliton generation by measuring at both the forward and backward ports. To verify the solitons to be stable and free of breathing oscillations, we photodetect a portion of the circuit output and monitor it using an electrical spectrum analyser. Figure 3b shows the primary, real-time signals of soliton formation in the case with a reflector and an optimal ϕ . As we scan α , we monitor P_b (red) and P_{comb}^b (blue). The soliton microcomb forms and stabilizes without an overly abrupt change in the intracavity power, mitigating thermal instability. Stabilizing a soliton with $R = 0$ is marginally more sensitive to system fluctuations, such as those of the on-chip pump power and pump detuning.

With the capability to form and measure solitons with nearly arbitrary settings of R and ϕ , we present predictions of laser power consumption and CE, emphasizing how the reflector closes off excess loss in the forward direction and enables near-unit CE. We plot predictions for P_f/P_{pump} (solid red line), P_b/P_{pump} (dashed red line) and CE (solid blue line) as a function of K in Fig. 3c. Here, the behaviour with K is important because power flows in our circuit through several channels: the

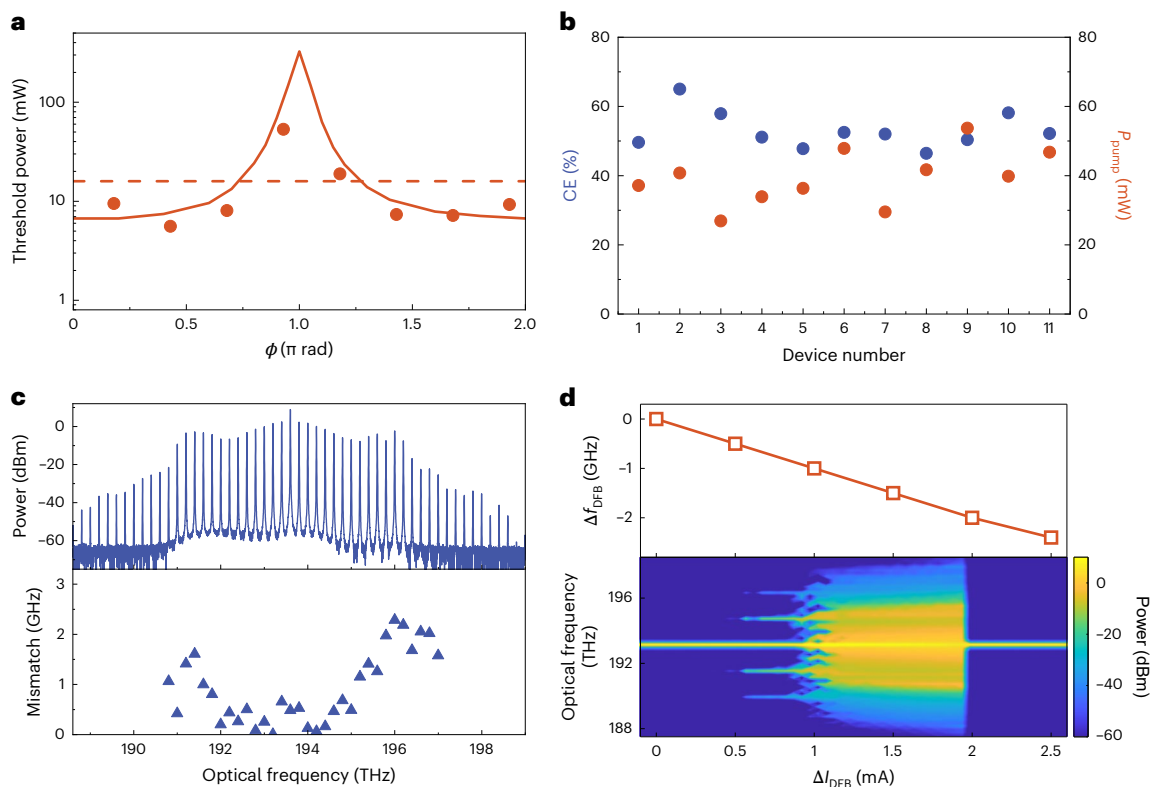


Fig. 4 | Practical characteristics of the nanophotonic circuit. a, Comparison between the measured (red circles) and simulated (solid red curve) threshold power versus ϕ in the nanophotonic circuit. The dashed red line represents that of a PhCR with the same parameters, except $R = 0$. **b**, Measured CE (filled blue circles) and P_{pump} (filled red circles) of 11 nanophotonic circuit devices on a single

chip. **c**, The optical spectrum of a 200 GHz soliton microcomb (upper panel) and its frequency mismatch with ITU-T grid (lower panel). **d**, Frequency tuning of the DFB laser from 193.1 THz (upper panel) and the associated spectrum generated by the nanophotonic circuit (lower panel) as we increase the laser current from 117 mA.

internal losses of the PhCR; through coherent scattering to balance the bidirectional PhCR; and the forward and backward output ports. Moreover, we optimize α to obtain the maximum CE at each setting of K and P_{pump} . The ratio of unused pump power, $(P_f + P_b)/P_{\text{pump}}$, indicates laser consumption in our nanophotonic circuit as shown by the red shaded area in Fig. 3c. The limit of $K \gg 1$, which we consider below, simplifies understanding because the internal losses can be neglected.

Now we directly compare the effect of the reflector. In the scenario in which $R = 0$ (upper panels of Fig. 3c), P_b is loaded by conversion to the soliton and P_f , and it contains about 25% of the pump for $K \gg 1$. At most, 50% of the pump is converted to the soliton, indicating clamped CE from the excess output of double-sided emission. Indeed, our measurements of CE versus K (blue circles in Fig. 3c) confirm the simulation. With the reflector set to $R = 0.9$, P_f is greatly reduced for all values of K (refer to the lower panels of Fig. 3c). Moreover, the backward pump inside the resonator is enhanced because we set ϕ for optimal constructive interference in both the measurements and the simulation. With appropriate P_{pump} and α , this unidirectional nanophotonic circuit enables conversion of the enhanced backward pump to the soliton microcomb, consuming, in principle, all of the input power. Moreover, the ratio of unused pump power exhibits a rapid decrease with K , reaching 0.2 at $K = 2$. Even larger values of K reduce the ratio of unused pump power to below 0.1 and increase the simulated CE to 87%, which is ultimately limited by the intrinsic loss of the resonator and non-unit R of the reflector. The panels labelled 1 and 2 on the right side of Fig. 3c show optical spectra of backward-propagating soliton microcombs that correspond to the CE measurements. In both cases, we observe an approximately constant power per mode: there are 20 comb modes with spectral power variation below 10 dB. Particularly, in panel 2, the nanophotonic circuit can generate 14 comb lines with power above 0.5 mW at $P_{\text{pump}} = 33$ mW.

Moreover, the pump mode is 20 dB lower than the adjacent comb lines, indicating high laser power consumption.

As our nanophotonic circuit generates a soliton microcomb with favourable properties for applications, we study some of its practical characteristics, including the operating power, the device yield in fabrication and the compatibility with a DFB laser diode as the pump source (see Fig. 4). The reflector phase also influences the threshold power for optical parametric oscillation, the precursor of soliton formation, since an optimal setting of ϕ maximally enhances the intracavity pump. Figure 4a shows measurements (red circles) and the LLE simulation (solid red line) of threshold power versus ϕ with the reflector. In this experiment, we undercouple the resonator with $K = 0.5$ to emphasize the reduced threshold power in our nanophotonic circuit while other parameters of the devices are the same as that in Fig. 3. The threshold power for a PhCR without a reflector (dashed red line in Fig. 4a) is a factor of 2.9 higher than the optimal reflector circuit, since the pump power is bidirectionally distributed not only inside the PhCR but also in the coupling waveguide.

The capability to yield a large fraction of fabricated nanophotonic circuits is an important consideration for applications. In particular, fabrication imprecision can degrade performance due to the sensitivity of ϕ and K to device geometry. We study this by testing several devices to assess variation of CE and the P_{pump} setting used to operate the circuit (Fig. 4b). Here we select eleven nanophotonic circuit devices on a single chip; all of the devices that we fabricate are operational but the designed parameter variations lead to reduced yield. Among the devices, CE varies around 50% and P_{pump} needed for operation varies around 40 mW. These values are consistent with our overall observed tolerance, and we optimize the fabrication procedure and scanning electron microscopy inspection to maintain a consistent K .

Beyond CE, microcomb applications also benefit from frequency alignment to the ITU-T grid—the international channel standard for data communication systems. Such alignment ensures compatibility with system components such as wavelength-division multiplexers and demultiplexers³¹. We demonstrate robust frequency alignment of the soliton microcomb generated in our nanophotonic circuit. In Fig. 4c we show the optical spectrum of a soliton microcomb with a precise 200 GHz mode spacing. By varying α and the ring width of the PhCR, we finely tune its FSR towards a target of 200 GHz and align ω_0 with any pre-defined grid. We present measurements of the frequency mismatch in Fig. 4c, in which the 27 microcomb modes between 191 THz and 197 THz are aligned to the ITU-T grid with accuracies better than 2.6 GHz.

To demonstrate the compatibility of our nanophotonic circuit with chip-scale lasers, we use a standard, butterfly packaged DFB laser as the pump (Fig. 4d). Such DFB lasers offer frequency adjustment through the control of laser temperature and current; specifically, the frequency-control parameters of our laser are -11.3 GHz K^{-1} and -0.9 GHz mA^{-1} , respectively. We therefore tune the DFB laser temperature to coarsely align the laser with the split mode, and then use the DFB laser current to sweep α for soliton generation. Figure 4d illustrates the DFB laser frequency change (Δf_{DFB}) with current and the associated spectrum generated by the nanophotonic circuit. We observe optical parametric oscillation followed by the evolution to a stable soliton. This straightforward and reliable technique combined with low required pump power and high CE of our nanophotonic circuits points the way to a scalable, frequency-comb laser source for high-capacity telecommunication applications.

In conclusion, we have presented a nanophotonic resonator circuit that consists of a bidirectional Kerr resonator and a reflector on the coupling waveguide. Coherent backscattering with nanophotonics enables arbitrary phase-matching and high laser power consumption in the normal-dispersion PhCRs, allowing for soliton formation at approaching unit CE. Using this nanophotonic circuit, we generate 200 GHz flat-top solitons with up to 65% CE and 97% pump consumption. We investigate the nonlinear dynamics and steady-state fields in the nanophotonic circuit with LLE, observing agreement between simulations and experimental measurements. Moreover, we study some practical characteristics of the nanophotonic circuit by demonstrating high yield fabrication of the high-efficiency devices, generation of comb lines that are precisely aligned with ITU-T frequency grids, and the compatibility with a chip-scale DFB pump laser for future integration^{32,52}. Although 54% CE has been achieved in anomalous dispersion microresonators³⁷, our work demonstrates a completely different approach for higher CEs in bidirectional Kerr resonators with normal dispersion. Compared with the work in ref. 37, our nanophotonic circuit offers several advantages such as a wider range of pump power and detuning for high CE (see Supplementary Fig. 4), much easier access to the single soliton state (see Supplementary Fig. 5), and better energy concentration in comb spectrum. We also systematically investigate the parameters affecting CE, particularly K , and demonstrate a reliable route to achieving near-unit CE. Furthermore, our design is robust against fabrication uncertainties and does not require post-fabrication tuning with on-chip heaters, even in the mass production of high-efficiency devices. Our work therefore represents a major advancement in developing microcombs with substantial output power to directly support a wide range of applications.

Online content

Any methods, additional references, Nature Portfolio reporting summaries, source data, extended data, supplementary information, acknowledgements, peer review information; details of author contributions and competing interests; and statements of data and code availability are available at <https://doi.org/10.1038/s41566-025-01624-1>.

References

- Willner, A. E., Khaleghi, S., Chitgarha, M. R. & Yilmaz, O. F. All-optical signal processing. *J. Lightwave Technol.* **32**, 660–680 (2014).
- Carlson, D. R. et al. Ultrafast electro-optic light with subcycle control. *Science* **361**, 1358–1363 (2018).
- Hansryd, J., Andrekson, P., Westlund, M., Li, J. & Hedekvist, P.-O. Fiber-based optical parametric amplifiers and their applications. *IEEE J. Sel. Topics Quant. Electron.* **8**, 506–520 (2002).
- Foster, M. A. et al. Broad-band optical parametric gain on a silicon photonic chip. *Nature* **441**, 960–963 (2006).
- Riemensberger, J. et al. A photonic integrated continuous-travelling-wave parametric amplifier. *Nature* **612**, 56–61 (2022).
- Dutt, A. et al. On-chip optical squeezing. *Phys. Rev. Appl.* **3**, 044005 (2015).
- Reimer, C. et al. Generation of multiphoton entangled quantum states by means of integrated frequency combs. *Science* **351**, 1176–1180 (2016).
- Yang, Z. et al. A squeezed quantum microcomb on a chip. *Nat. Commun.* **12**, 4781 (2021).
- Guidry, M. A., Lukin, D. M., Yang, K. Y., Trivedi, R. & Vučković, J. Quantum optics of soliton microcombs. *Nat. Photon.* **16**, 52–58 (2022).
- Jahanbozorgi, M. et al. Generation of squeezed quantum microcombs with silicon nitride integrated photonic circuits. *Optica* **10**, 1100–1101 (2023).
- Kippenberg, T. J., Holzwarth, R. & Diddams, S. A. Microresonator-based optical frequency combs. *Science* **332**, 555–559 (2011).
- Moss, D. J., Morandotti, R., Gaeta, A. L. & Lipson, M. New CMOS-compatible platforms based on silicon nitride and hydrex for nonlinear optics. *Nat. Photon.* **7**, 597–607 (2013).
- Pasquazi, A. et al. Micro-combs: a novel generation of optical sources. *Phys. Rep.* **729**, 1–81 (2018).
- Kippenberg, T. J., Gaeta, A. L., Lipson, M. & Gorodetsky, M. L. Dissipative Kerr solitons in optical microresonators. *Science* **361**, eaan8083 (2018).
- Gaeta, A. L., Lipson, M. & Kippenberg, T. J. Photonic-chip-based frequency combs. *Nat. Photon.* **13**, 158–169 (2019).
- Ji, X. et al. Ultra-low-loss on-chip resonators with sub-milliwatt parametric oscillation threshold. *Optica* **4**, 619–624 (2017).
- Lu, X., Moille, G., Rao, A., Westly, D. A. & Srinivasan, K. On-chip optical parametric oscillation into the visible: generating red, orange, yellow, and green from a near-infrared pump. *Optica* **7**, 1417–1425 (2020).
- Black, J. A. et al. Optical-parametric oscillation in photonic-crystal ring resonators. *Optica* **9**, 1183–1189 (2022).
- Perez, E. F. et al. High-performance Kerr microresonator optical parametric oscillator on a silicon chip. *Nat. Commun.* **14**, 242 (2023).
- Herr, T. et al. Temporal solitons in optical microresonators. *Nat. Photon.* **8**, 145–152 (2014).
- Yi, X., Yang, Q.-F., Yang, K. Y., Suh, M.-G. & Vahala, K. Soliton frequency comb at microwave rates in a high-Q silica microresonator. *Optica* **2**, 1078–1085 (2015).
- Xu, G. et al. Spontaneous symmetry breaking of dissipative optical solitons in a two-component Kerr resonator. *Nat. Commun.* **12**, 4023 (2021).
- Yu, S.-P. et al. Spontaneous pulse formation in edgeless photonic crystal resonators. *Nat. Photon.* **15**, 461–467 (2021).
- Yu, S.-P., Lucas, E., Zang, J. & Papp, S. B. A continuum of bright and dark-pulse states in a photonic-crystal resonator. *Nat. Commun.* **13**, 3134 (2022).

25. Lucas, E., Yu, S.-P., Briles, T. C., Carlson, D. R. & Papp, S. B. Tailoring microcombs with inverse-designed, meta-dispersion microresonators. *Nat. Photon.* **17**, 943–950 (2023).
26. Shen, B. et al. Integrated turnkey soliton microcombs. *Nature* **582**, 365–369 (2020).
27. Voloshin, A. S. et al. Dynamics of soliton self-injection locking in optical microresonators. *Nat. Commun.* **12**, 235 (2021).
28. Xiang, C. et al. Laser soliton microcombs heterogeneously integrated on silicon. *Science* **373**, 99–103 (2021).
29. Briles, T. C. et al. Hybrid InP and SiN integration of an octave-spanning frequency comb. *APL Photon.* **6**, 026102 (2021).
30. Ulanov, A. E. et al. Synthetic reflection self-injection-locked microcombs. *Nat. Photon.* **18**, 294–299 (2024).
31. Yang, K. Y. et al. Multi-dimensional data transmission using inverse-designed silicon photonics and microcombs. *Nat. Commun.* **13**, 7862 (2022).
32. Rizzo, A. et al. Massively scalable Kerr comb-driven silicon photonic link. *Nat. Photon.* **17**, 781–790 (2023).
33. Tan, M. et al. Photonic RF and microwave filters based on 49 GHz and 200 GHz Kerr microcombs. *Optics Commun.* **465**, 125563 (2020).
34. Xue, X., Zheng, X. & Zhou, B. Super-efficient temporal solitons in mutually coupled optical cavities. *Nat. Photon.* **13**, 616–622 (2019).
35. Bao, H. et al. Laser cavity-soliton microcombs. *Nat. Photon.* **13**, 384–389 (2019).
36. Cole, D. C., Lamb, E. S., Del'Haye, P., Diddams, S. A. & Papp, S. B. Soliton crystals in Kerr resonators. *Nat. Photon.* **11**, 671–676 (2017).
37. Helgason, Ó. B. et al. Surpassing the nonlinear conversion efficiency of soliton microcombs. *Nat. Photon.* **17**, 992–999 (2023).
38. Girardi, M., Helgason, Ó. B., Ortega, C. H. L., Rebolledo-Salgado, I. & Torres-Company, V. Superefficient microcombs at the wafer level. Preprint at <https://arxiv.org/abs/2309.02280> (2023).
39. Xue, X. et al. Mode-locked dark pulse kerr combs in normal-dispersion microresonators. *Nat. Photon.* **9**, 594–600 (2015).
40. Xue, X., Wang, P.-H., Xuan, Y., Qi, M. & Weiner, A. M. Microresonator Kerr frequency combs with high conversion efficiency. *Laser Photon. Rev.* **11**, 1600276 (2017).
41. Kim, B. Y. et al. Turn-key, high-efficiency Kerr comb source. *Opt. Lett.* **44**, 4475–4478 (2019).
42. Helgason, Ó. B. et al. Dissipative solitons in photonic molecules. *Nat. Photon.* **15**, 305–310 (2021).
43. White, A. D. et al. Integrated passive nonlinear optical isolators. *Nat. Photon.* **17**, 143–149 (2023).
44. Bogaerts, W. et al. Silicon-on-insulator spectral filters fabricated with cmos technology. *IEEE J. Sel. Top. Quantum Electronics* **16**, 33–44 (2010).
45. Dai, D. Silicon nanophotonic integrated devices for on-chip multiplexing and switching. *J. Lightwave Technol.* **35**, 572–587 (2017).
46. Lamee, K. F., Carlson, D. R., Newman, Z. L., Yu, S.-P. & Papp, S. B. Nanophotonic tantalum waveguides for supercontinuum generation pumped at 1560 nm. *Optics Lett.* **45**, 4192–4195 (2020).
47. Jung, H. et al. Tantalum kerr nonlinear integrated photonics. *Optica* **8**, 811–817 (2021).
48. Black, J. A. et al. Group-velocity-dispersion engineering of tantalum integrated photonics. *Optics Lett.* **46**, 817–820 (2021).
49. Lugiato, L. A. & Lefever, R. Spatial dissipative structures in passive optical systems. *Phys. Rev. Lett.* **58**, 2209–2211 (1987).
50. Skryabin, D. V. Hierarchy of coupled mode and envelope models for bi-directional microresonators with kerr nonlinearity. *OSA Continuum* **3**, 1364–1375 (2020).
51. Liu, H. et al. Threshold and laser conversion in nanostructured-resonator parametric oscillators. *Phys. Rev. Lett.* **132**, 023801 (2024).
52. Shirpurkar, C. et al. Photonic crystal resonators for inverse-designed multi-dimensional optical interconnects. *Optics Lett.* **47**, 3063–3066 (2022).

Publisher's note Springer Nature remains neutral with regard to jurisdictional claims in published maps and institutional affiliations.

Springer Nature or its licensor (e.g. a society or other partner) holds exclusive rights to this article under a publishing agreement with the author(s) or other rightsholder(s); author self-archiving of the accepted manuscript version of this article is solely governed by the terms of such publishing agreement and applicable law.

© The Author(s), under exclusive licence to Springer Nature Limited 2025

Methods

Reflector characterization

We measure the reflector transmission using broad-band amplified spontaneous emission (ASE) noise from a semiconductor optical amplifier as the light source. Given that the reflector transmission depends on the polarization state of the incident light, we use a fibre polarizer after the SOA to achieve polarized ASE noise and optimize its polarization with a fibre polarization controller. The optical spectrum of the PhCR chip output is monitored by an optical spectrum analyser, providing a reference for optimizing the ASE noise polarization. We can calculate the transmission profile of the reflector by comparing the optical spectra at the input and output of the PhCR chip and subtracting the fibre coupling loss (see Fig. 2c).

Aligning comb lines with ITU-T frequency grids

We align the microcomb with ITU-T frequency grids by fabricating multiple devices with varying ring radius and ring width, followed by fine-tuning of the chip temperature. Both the pump mode frequency and comb line spacing depends on the geometric parameters but the former is more sensitive, which allows us to tune pump mode frequency without notable change of the comb line spacing. Operationally, we first design multiple devices with linear scan of ring radius to achieve a comb line spacing of 200 GHz (tuning rate = $-1.82 \text{ MHz nm}^{-1}$). We then fix the ring radius and scan ring width so that the pump mode is aligned with one of the ITU-T frequency grids. For the 200 GHz devices used in our experiment, the tuning rate of the pump mode frequency is -2.3 GHz nm^{-1} . Next, we change the device temperature by using a thermoelectric cooler to finely tune the pump mode frequency (tuning rate $\approx -1 \text{ GHz per } ^\circ\text{C}$) and further reduce the potential mismatch. Using this method, we demonstrate microcombs with mismatch of 17 comb modes below 2.6 GHz.

Data availability

Source Data are provided with this paper. Further data are available from the corresponding author on reasonable request.

Code availability

The simulation codes used in this study are available from the corresponding author on reasonable request.

Acknowledgements

We thank A. Dan and Y. Li for reading the manuscript. This work is a contribution of NIST and not subject to US copyright. This research has been funded by DARPA PIPES (J.Z., S.-P.Y., H.L., Y.J., S.B.P.), AFOSR FA9550-20-1-0004 project no. 19RT1019 (S.B.P.), NSF Quantum Leap Challenge Institute Award OMA-2016244 (S.B.P.), and NIST on a Chip (S.B.P.). Mention of specific companies or trade names is for scientific communication only and does not constitute an endorsement by NIST.

Author contributions

S.-P.Y. conceived the experiment. S.-P.Y. and J.Z. designed the nanophotonic circuit. J.Z. performed the optical measurements and numerical simulations. H. L. and Y. J. contributed to the theoretical understanding. T.C.B. and D.R.C. fabricated the nanophotonic circuits. S.B.P. contributed to the theoretical understanding and supervised the project. J.Z. and S.B.P. analysed the data and wrote the manuscript. All authors reviewed the results and provided feedback on the manuscript.

Competing interests

The authors declare no competing interests.

Additional information

Supplementary information The online version contains supplementary material available at <https://doi.org/10.1038/s41566-025-01624-1>.

Correspondence and requests for materials should be addressed to Jizhao Zang.

Peer review information *Nature Photonics* thanks Xiaoxiao Xue and the other, anonymous, reviewer(s) for their contribution to the peer review of this work.

Reprints and permissions information is available at www.nature.com/reprints.